Dynamics of pit filling in heteroepitaxy via phase-field simulations

Marco Albani, Roberto Bergamaschini,* and Francesco Montalenti
L-NESS and Department of Materials Science, University of Milano-Bicocca, Via R. Cozzi 55, I-20125 Milano, Italy
(Received 21 April 2016; revised manuscript received 7 July 2016; published 5 August 2016)

Heteroepitaxial growth on a pit-patterned substrate is investigated by phase-field simulations, tackling both film and substrate geometry and elastic properties. The dynamics results from material deposition and redistribution via surface diffusion according to the tendency toward free-energy minimization. The balance between surface energy, misfit strain, and wetting effects is taken into account. Numerical solution by finite-element method permits to properly account for the role played by the actual pit morphology in determining strain relaxation. The mechanisms leading to island growth into the pit are discussed. Different growth parameters and pattern geometries are considered and their effects on island ordering are explained and related to experimental evidences in literature.

DOI: 10.1103/PhysRevB.94.075303

I. INTRODUCTION

Islanding phenomena in semiconductor heteroepitaxy have been the object of deep investigation since decades [1–4]. The general understanding of the growth mechanism was successfully provided by the well-known Asaro-Tiller-Grinfeld (ATG) instability model [5–7]. In the absence of nucleation barriers [8], the ATG theory explains how strained films can become unstable against profile perturbations, leading to island formation. The driving force of the process lays in the competition between surface energy costs, favoring flattening, and relaxation of elastic strain, inducing roughening. Numerous efforts have been devoted to make the approach more effective in capturing the details of the growth process [9] by including wetting-energy contributions [10–13], surface anisotropy [13,14], entropy of mixing between the alloy components [15–18], or even plastic effects [19].

The need to control positioning and size of islands for technological purposes drove the research toward substrate prepatterning. A common approach consists in patterning the substrate with ordered arrays of pits. Nowadays, reactive ion etching and lithographic techniques [20,21] permit an accurate control on the definition of the pattern, allowing for the formation of nanometric pits with different size and morphology. It has been widely proved [4,22–26] that, under suitable growth conditions, perfectly ordered islands can be obtained, with striking size and shape homogeneity. However, only a narrow window of parameters yields such an ideal behavior [27,28]. Growth temperature and deposition flux as well as pit size, shape, and periodicity all affect the localization and uniformity of the grown islands.

Several studies are reported in literature [18,24,29–31] inspecting the role of the pits in directing the growth. From one side, a general tendency toward filling the pit is expected due to capillarity. On the other hand, the strain relaxation of islands into the pits differs from the condition of flat substrate [32], thus changing the surface versus elastic energy balance, at the basis of the ATG instability model. An "exact" treatment of this latter contribution is computationally quite demanding so that, typically, approximated approaches are implemented, restricting the description to selected shapes [30,33,34].

In this work, a general phase-field (PF) approach aimed at modeling island growth [35,36] on patterned substrates is introduced. In particular, the method profits of the possibility to implicitly track both the film free surface and the substrate interface by means of two different order parameters. A set of partial differential equations (PDE) is then derived, coupling the strain relaxation and the evolution of the profile. The solution of this time-dependent problem by finite-element method (FEM) allows one to deal with whatever complex morphology, including the ones typically seen in actual experiments.

Growth simulations are performed in order to identify the mechanisms driving the island localization and to inspect how the growth parameters might affect them. The prototypical system Ge/Si(001) (within the approximation of isotropic surface energy and elastic properties, and neglecting intermixing effects) will be considered as a reference case, but most of the conclusions are expected to be valid for a wide range of Stranski-Krastanov (SK) systems, such as III-V compounds [3,37]. The results are rationalized with respect to the evolution of the wetting layer (WL) during deposition.

The paper is organized as follows. In Sec. II, the PF model, based on the coupling of the surface diffusion dynamics with the calculation of the strain field, is introduced. Wetting-energy contributions, crucial for the description of the substrate-film interface, are introduced in Sec. II A. Simulation results follow in Sec. III. First, the mechanisms leading to island localization into the pit are investigated (Sec. III A). Then, in Sec. III B, different growth conditions are considered and their impact on the evolution is assessed. Different pit geometries and materials are also discussed in Sec. III C. For the sake of simplicity, these analyses are referred to two-dimensional (2D) systems. The effects of considering a full three-dimensional (3D) geometry are discussed in Sec. III D, preceding conclusions.

II. METHOD

In this work, the phase-field model of surface diffusion proposed by Rätz *et al.* in Ref. [36] is extended to the simulation of island growth on pit-patterned substrates, following the approach of Ref. [38] (see also Refs. [14,39,40]). To this purpose, the three-phases system formed by substrate,

*roberto.bergamaschini@mater.unimib.it

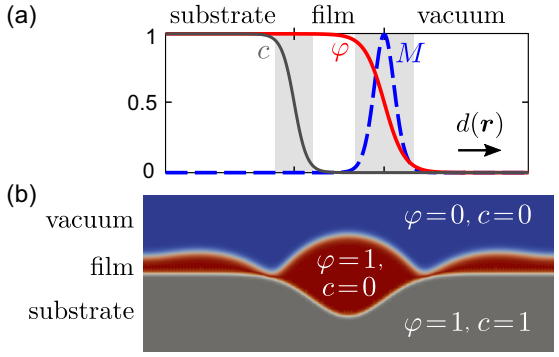

FIG. 1. System representation by the PF approach. (a) Plot of the phase-field functions φ and c and of the surface mobility $M(\varphi,c)$ (scaled to unity) with respect to the signed distance $d(\boldsymbol{r})$ from the surface and substrate profiles. Shaded regions correspond to the diffuse interfaces. (b) Definition of the substrate-film-vacuum regions by the φ and c fields within the simulation cell.

film, and vacuum is considered. As illustrated in Fig. 1, two phase-field functions φ and c are used to distinguish between the different regions. φ is set to vary smoothly from 1 in the solid to 0 in the vacuum, thus providing an implicit tracking of the free-surface profile, represented by the diffuse interface in-between these bulk regions, localized at the $\varphi = 0.5$ isoline (used in the figures to trace the surface profile). The field c is set to 1 in the substrate and 0 elsewhere, tracing the film-substrate boundary at $c = 0.5$. No substrate-vacuum interface is taken into account as the present description is limited to the case of SK growth, namely, Ge on Si, where the film always forms a thin WL on top of the substrate. A suitable definition of the phase-field function, used for both φ and c, is given by $1/2\{1 - \tanh[3d(\boldsymbol{r})/\epsilon]\}$ [see Fig. 1(a)], with ϵ the amplitude of the interface region and $d(\boldsymbol{r})$ the signed distance of a generic point $\boldsymbol{r}$ from the actual profile.

The growth process can be modeled by considering material deposition and redistribution along the surface. Bulk diffusion is assumed to be negligible due to high activation barriers. For the same reason, the substrate, located within the solid bulk by construction, does not evolve in time (t), i.e., $\partial c/\partial t = 0$. This is especially true when considering Si as a substrate, due to its rather low mobility compared to Ge [41]. Actually, experimental and theoretical studies [16,42] showed that intermixing effects might play a role when dealing with few monolayers (ML) thick films and sufficiently high temperatures. In particular, Ge deposition was observed to activate Si diffusion along the surface, leading to significant variations in the pit shape [18], here neglected.

In the assumption of quasiequilibrium conditions, the net flow of matter along the surface results from the tendency toward free-energy minimization, following the local gradients of chemical potential μ [43,44]. In the PF framework, the evolution of the film profile is directly traced by the temporal variation of the φ field itself, here defined by the degenerate Cahn-Hilliard equation for the surface-diffusion process, with an additional source term $F(\varphi)$, corresponding to the deposition flux:

$$\frac{\partial \varphi}{\partial t} = \nabla \cdot [M(\varphi,c)\, \nabla \mu] + F(\varphi). \tag{1}$$

The mobility function $M(\varphi,c) = D(36/\epsilon)(1-c)\varphi^2(1-\varphi)^2$, restricted at the film surface region as shown in Fig. 1(a), is considered. D is an effective diffusion coefficient, setting the absolute time scale. Equation (1) enforces a conservative dynamics with no loss/gain of material, except for the deposition term.

A vertical and uniform deposition flux $\boldsymbol{f} = -f\hat{\boldsymbol{z}}$, mimicking the conditions of molecular beam epitaxy, is assumed:

$$F(\varphi) = -(1+\mathcal{R})\, \boldsymbol{f} \cdot \nabla \varphi = -(1+\mathcal{R})\, f \frac{\partial \varphi}{\partial z}, \tag{2}$$

where f is the nominal deposition flux and $\mathcal{R} \in [-1,1]$ is a random number, introduced to simulate local beam fluctuations (and to trigger the profile instability).

The chemical potential can be derived from the total free energy G as $\mu = \delta G/\delta\varphi$. G is given in the form of a Ginzburg-Landau functional:

$$G[\varphi] = \int_\Omega \gamma \left(\frac{\epsilon}{2} |\nabla \varphi|^2 d\boldsymbol{r} + \frac{1}{\epsilon} B(\varphi) \right) d\boldsymbol{r} + \int_\Omega \rho[\varphi,c,\boldsymbol{u}] d\boldsymbol{r}, \tag{3}$$

where $B(\varphi) = 18\varphi^2(1-\varphi)^2$ is a double-well potential. The first term is the surface energy, determined by the surface energy density γ, here assumed to be independent of the local orientation. The second term is the elastic contribution defined by the elastic energy density $\rho[\varphi,c,\boldsymbol{u}]$, dependent on the surface and substrate morphologies (through φ and c) and on the displacement field $\boldsymbol{u}$. The latter describes the local lattice deformation $\boldsymbol{u} = \boldsymbol{u}(\boldsymbol{r})$ due to the film-substrate misfit strain $\varepsilon_{\mathrm{m}}^{\mathrm{fs}} = (a_{\mathrm{s}} - a_{\mathrm{f}})/a_{\mathrm{f}}$, with a_{s} and a_{f} the lattice parameters of the substrate and film, respectively. For Ge/Si, $\varepsilon_{\mathrm{m}}^{\mathrm{fs}} = -0.0399$. By considering an elastically isotropic medium and introducing the local elastic strain tensor $\boldsymbol{\varepsilon}$, such that $\varepsilon_{ij} = \frac{1}{2}(\partial u_i/\partial x_j + \partial u_j/\partial x_i) + \varepsilon_{\mathrm{m}}\delta_{ij}$, ρ is given by

$$\rho = \mu \sum_{i,j} \varepsilon_{ij}^2 + \frac{\lambda}{2}[\mathrm{tr}(\boldsymbol{\varepsilon})]^2. \tag{4}$$

The misfit ε_{m} and the Lamé coefficients μ, λ are extended to the overall domain Ω by means of an interpolation function $h(\varphi) = \varphi^3(6\varphi^2 - 15\varphi + 10)$, modulating their values from the ones of the substrate (at zero misfit and with elastic constants μ_{s}, λ_{s}) to those of the film ($\varepsilon_{\mathrm{m}}^{\mathrm{fs}}$, μ_{f}, λ_{f}) by means of c:

$$\begin{aligned} \varepsilon_{\mathrm{m}} &= (1-c)\varepsilon_{\mathrm{m}}^{\mathrm{fs}} h(\varphi), \\ \mu &= [c\mu_{\mathrm{s}} + (1-c)\mu_{\mathrm{f}}]h(\varphi) + \mu_{\mathrm{v}}, \\ \lambda &= [c\lambda_{\mathrm{s}} + (1-c)\lambda_{\mathrm{f}}]h(\varphi), \end{aligned} \tag{5}$$

where μ_{v} is a small number $\sim 10^{-6}$ GPa, introduced for numerical reasons only [36]. The convenience of our approach is then twofold as it permits to tackle whatever complex film and substrate geometries, exploiting the implicit description via φ and c, and to properly account for the different elastic properties of the corresponding materials. This latter feature, almost negligible for the prototypical SiGe system ($\mu_{\mathrm{Si}} = 52$ GPa, $\lambda_{\mathrm{Si}} = 60$ GPa while $\mu_{\mathrm{Ge}} = 41$ GPa, $\lambda_{\mathrm{Ge}} = 44$ GPa), can play quite a role for other heteroepitaxial systems or in the case of compliant substrates recently reported in the literature [45].

In order to define the elastic contribution to the system free energy, the displacements $\boldsymbol{u}$ must be determined. In principle, this could be performed by coupling Eq. (1), describing the system evolution, with an equation for the strain relaxation process. However, the typical time scale for the diffusion processes is much larger than the one for the elastic deformation so that mechanical equilibrium can be assumed to hold at any time with respect to Eq. (1). The problem of mechanical equilibrium of an elastic solid is a rather standard one and is set by considering the zero-forces condition, that in differential form reads as $\nabla \cdot \boldsymbol{\sigma} = \mathbf{0}$, with the stress tensor $\boldsymbol{\sigma}$ given by $\sigma_{ij} = 2\mu\varepsilon_{ij} + \delta_{ij}\lambda \mathrm{tr}(\boldsymbol{\varepsilon})$, based on the Hooke's law. A PDE for the equilibrium displacement field $\boldsymbol{u}$ can then be written in tensor form as

$$\nabla \cdot [\mu(\nabla \boldsymbol{u} + (\nabla \boldsymbol{u})^T)] + \nabla(\lambda \nabla \cdot \boldsymbol{u}) = \nabla[(2\mu + 3\lambda)\varepsilon_{\mathrm{m}}]. \quad (6)$$

The numerical solution of Eq. (6) for a representative case of a Ge island grown into a Si pit is reported in Fig. 2. Dirichlet boundary conditions are enforced at the bottom of the cell (Γ_D), where the lattice is assumed to be not deformed, i.e., $\boldsymbol{u} = \mathbf{0}$. If the solid region were defined explicitly, Neumann boundary conditions $\boldsymbol{\sigma} \cdot \hat{\boldsymbol{n}} = \mathbf{0}$ should be applied at the free surfaces (Γ_N), but in the phase-field approach these are automatically included by considering the extension of the elastic problem to the vacuum region. Periodic boundary conditions (PBC) are set on the lateral boundaries of the integration domain. In Fig. 2(b), on the left-hand side, the solution of the strain field component ε_{xx} is shown on the overall domain for a 2D slice through the island center. On the right-hand side, the unphysical region corresponding to vacuum is clipped away, leaving only the solid below $\varphi = 0.5$. Notice that within the interface the values of the strain field are influenced by the modulation of the misfit strain ε_{m} due to the $h(\varphi)$ function, highlighted in the figure. This is fully consistent with the diffused description of the surface and converges to the expected value in the sharp-interface limit, i.e., when $\epsilon \to 0$. For the sake of readability, in the 3D perspective views, the profile is cut at the $\varphi = 0.9$ isoline, $\sim\epsilon/2$ below the nominal surface, in order to exclude from the plot the interface region affected by such modulation.

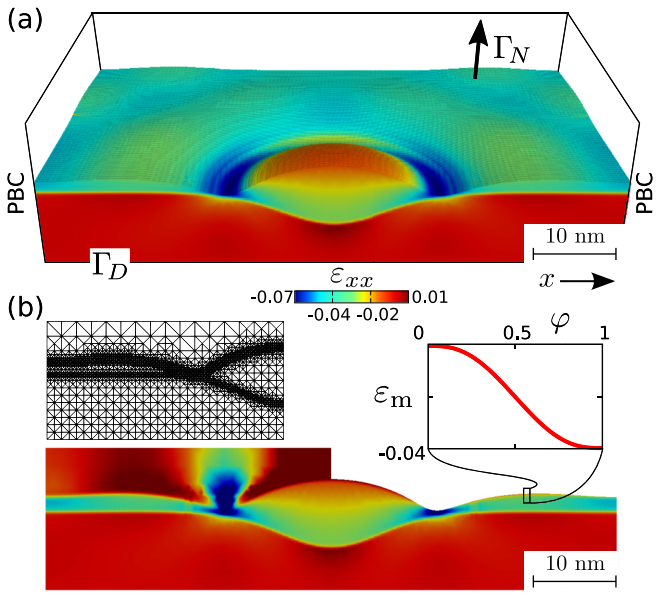

FIG. 2. Strain field calculation by PF. (a) Color map of the strain component ε_{xx} for a 3D Ge island on a pit-patterned Si substrate. Half of the simulation cell is reported to show the strain distribution within the film and the substrate in cross section. The surface is cut at $\varphi = 0.9$ in order to exclude the strain modulation due to the $h(\varphi)$ function. (b) Cross section through the island center showing the full map of the strain field including the vacuum region (left) and the corresponding cut below the surface profile at $\varphi = 0.5$ (right). The modulation of the misfit strain ε_{m} at the film-vacuum interface is highlighted. The mesh used in the FEM calculation (for half of the profile) is reported in the inset, showing the local refinement at the interfaces traced by both φ and c.

At each time step, the equilibrium strain field is calculated by solving Eq. (6) and plugged into Eq. (1) by the definition of the local chemical potential μ here provided:

$$g(\varphi)\mu = \gamma\left[-\epsilon\nabla^2\varphi + \frac{1}{\epsilon}\frac{\partial}{\partial\varphi}B(\varphi)\right] + \frac{\partial}{\partial\varphi}\rho(\varphi, c, \boldsymbol{u}), \quad (7)$$

where the stabilizing function $g(\varphi) = 30\varphi^2(1-\varphi)^2$ has been introduced to ensure a better convergence to the sharp-interface limit [36,46].

A. Wetting energy and critical thickness

The most peculiar feature of SK growth is the formation of a WL, few ML thick, on top of which the islands evolve. This is due to the lower surface energy of the material forming the film compared with the substrate, e.g., for Ge/Si [47] $\gamma_{\mathrm{Ge}} \approx 6.0\ \mathrm{eV/nm^2} < \gamma_{\mathrm{Si}} \approx 8.7\ \mathrm{eV/nm^2}$ and the interfacial energy is negligible. *Ab initio* calculations [37,48] also showed that the surface energy of the growing film is not constant, but depends on the film thickness h. This is well fitted [10–13] by an exponential decay from the surface energy density of the substrate γ_{s} at 0 ML to the one of the film γ_{f} in the limit of thick films:

$$\gamma(h) = \gamma_{\mathrm{f}} + (\gamma_{\mathrm{s}} - \gamma_{\mathrm{f}})\exp(-h/\delta). \quad (8)$$

A decay length $\delta \sim$ ML is used, such to return the bulk value γ_{f} when the film thickness exceeds 3–5 MLs.

The role of the wetting term in the modeling of island growth is twofold. First, it introduces a critical film thickness h_{c} below which the film, even if strained, is definitely stable. In a linear approximation, for biaxial strain and neglecting the difference in elastic constants, it is possible to estimate [13,49] $h_{\mathrm{c}} \approx -\delta \ln\{(U_\varepsilon^2\delta^2)/[4\gamma_{\mathrm{f}}(\gamma_{\mathrm{s}} - \gamma_{\mathrm{f}})]\}$, where $U_\varepsilon = \varepsilon_{\mathrm{m}}^2 2\mu_{\mathrm{f}}(2\mu_{\mathrm{f}} + 3\lambda_{\mathrm{f}})^2/[(\mu_{\mathrm{f}} + \lambda_{\mathrm{f}})(2\mu_{\mathrm{f}} + \lambda_{\mathrm{f}})]$. Second, the increased surface energy cost when approaching the substrate provides a regularization of the profile instability, limiting its tendency to dig deep trenches toward the substrate. The cusp singularities predicted by the standard (nonlinear) ATG model are avoided and islands are formed on top of a thin WL, reproducing the evidences of the SK growth mode. This way, simulations can tackle long-time scales, including the slow dynamics of coarsening between the islands [13].

The evolution of a flat film during deposition has been simulated with the present method. Results are reported in Fig. 3. A value of $\delta = 0.27$ nm is considered in all the simulations here reported, leading to a critical thickness $h_{\mathrm{c}} \approx 1.2$ nm. This slightly overestimates the value of 3–5 MLs

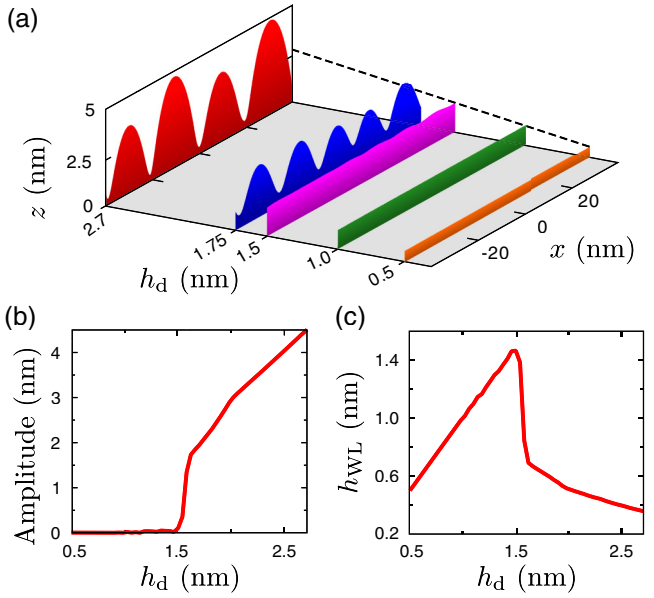

FIG. 3. 2D simulation of island growth on a flat substrate during deposition ($f/D = 8 \times 10^{-4}$). Time is represented by the deposited material h_d. (a) Evolution sequence for the film profile. (b) Maximum peak-to-valley amplitude of the film. (c) Minimum film thickness, corresponding to the WL height h_{WL}.

typically observed in experiments [50]. We shall accept this discrepancy as lowering δ leads to problems in meshing. As far as the film thickness h is lower than h_c, the flat profile remains stable against any perturbation, as made evident in Fig. 3(b), where the maximum amplitude of the profile is observed not to grow. Once the film thickness exceeds h_c, the film becomes unstable and a random perturbation, triggered by the fluctuations in the flux, starts to grow, similarly to the prediction of ATG model. However, it takes some time for the perturbation to reach an appreciable amplitude so that the apparent critical thickness [16,51] required to observe visible islands always exceeds the thermodynamic value h_c by an amount proportional to the deposition rate. Figure 3(c), reporting the variation in the WL thickness during the whole process, clearly shows an abrupt thinning of the WL (similar to the behavior reported in Ref. [52]), which occurs soon after the raise of the instability, when its growth rate becomes larger than the one of deposition. At this point, islands grow larger by digging trenches. However, this process is almost terminated by the wetting contribution as soon as a characteristic WL thickness $h_{WL} < h_c$ is reached. With the present parameters, $h_{WL} \approx 3$ ML, in agreement with the experimental observation for Ge/Si. As shown by the late evolution stages in Fig. 3(a), islands continue to grow on top of the WL capturing the additional material provided by the deposition. Coarsening effects [13] are finally observed, with material transfers favoring the largest islands, offering a better strain relaxation, as expected for Ostwald ripening.

B. Computational details

The model has been implemented using the FEM toolbox AMDiS [53,54], optimized for the phase-field approach. The FEM provides an exact numerical solution for both the diffusion dynamics and the mechanical equilibrium PDEs. As shown in the inset of Fig. 2(b), the geometry is defined by an adaptive mesh, finer at the free surface and at the film-substrate interface, where a higher precision is required, and coarser in the bulk regions, especially in the vacuum where the solution is nonphysical. The length scale considered in the simulations is that of nm so that, in order to provide well-localized interfaces still resolved by enough mesh points (at least 8 in our simulations), the widths ϵ of the free surface and of the film-substrate interface are set equal to 0.5 and 0.2 nm, respectively. As evident from Eq. (1), the time scale can be set arbitrarily with respect to D as $\tau = D^{-1}$. The actual value of D can be estimated as $D = h_l V_a D_0 (kT)^{-1} \exp[-E_b/(kT)]$, with h_l the ML thickness, V_a the volume per atom, D_0 the material diffusion coefficient, E_b the energy barrier for site hopping, k the Boltzmann constant, and T the temperature. More specifically, by considering the reference system Ge/Si, $h_l = 0.146$ nm, $V_a = 0.02$ nm^3, $D_0 = 8.5 \times 10^8$ nm^2/s [55], $E_b = 1.1$ eV [56], and a typical growth temperature $T = 650\,^\circ$C are assumed. With this parameter choice, $\tau \approx 0.03$ s, so that the duration of the deposition or annealing processes reproduced in the simulations is on a reasonable time scale of minutes. Actually, when considering the growth process, the key parameter is the relative time scale between deposition and diffusion, i.e., the f/D ratio.

A semi-implicit scheme is adopted for the time integration, with time linearization of the term $B'(\varphi)$ (see Ref. [57] for details). The time step is adapted dynamically during the simulations, with values ranging between 10^{-1}–$10^{-2}\tau$.

III. RESULTS AND DISCUSSION

The phase-field model here presented has been applied to investigate the mechanisms driving the growth of heteroepitaxial islands on pit-patterned substrates (Sec. III A). The role of the deposition flux versus surface mobility, with respect to the pit sizes and pattern periodicity, is discussed in Sec. III B. Effects related to the pit geometry and material properties, i.e., misfit strain and elastic constants, are investigated in Sec. III C. More realistic simulations, performed in a full 3D description, are reported in Sec. III D.

A. Island growth into the pit

In this section, optimal growth conditions are considered to understand the physics behind the growth of islands inside pits. To this goal, 2D simulations, representing the xz section (where z is the vertical direction) of a biaxially strained film, infinitely extended in the y direction, are considered. Pits are modeled as V-shaped trenches, with 1:6 aspect ratio (AR), defined as the height-to-base ratio. This roughly corresponds to the typical AR of the pits observed experimentally at the onset of island growth [28].

A typical evolution sequence obtained by a growth simulation is shown in Fig. 4(a). The initial profile consists of a 30-nm-wide pit, approximately two times larger than the instability wavelength $\lambda_{ATG} \approx 15$ nm expected from the ATG model, surrounded by a 50-nm flat region, corresponding to the pattern period (PBC are set). An initial, 0.5-nm-thick, Ge film, well below the critical thickness h_c, is set to conformally

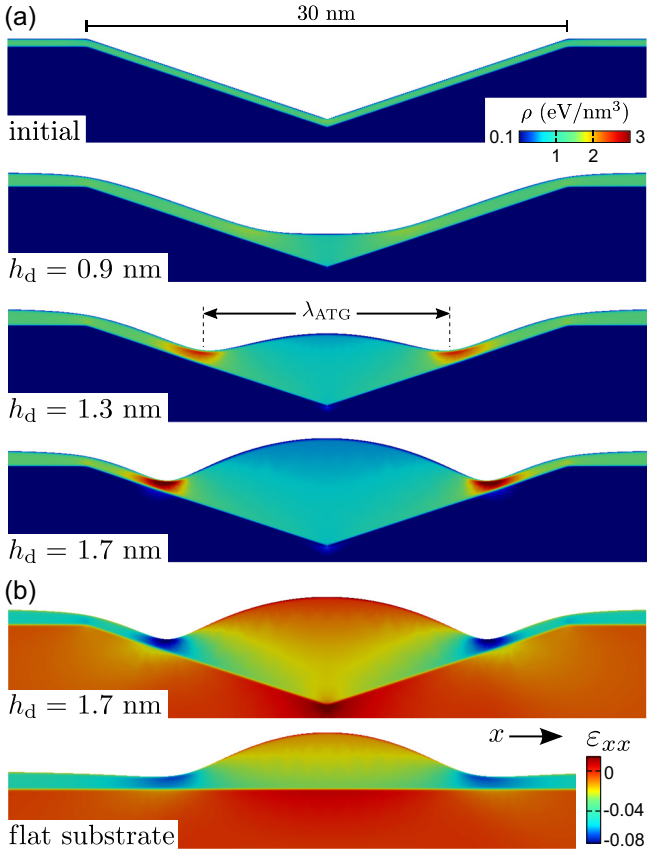

FIG. 4. Simulation of island growth into a pit. (a) Evolution sequence during deposition ($f/D = 4 \times 10^{-4}$). The first profile, corresponding to the initial condition for the simulation, is set as a conformal 0.5-nm-thick film. The color map for the elastic energy density ρ is shown. λ_{ATG} is reported as reference. (b) Comparison of the strain map of the ε_{xx} component between the island grown into the pit and an equivalent one, with the same base and height, formed on a flat substrate. Only a portion of the 80-nm-wide cell is reported. Figures are in 1:1 ratio.

cover the substrate. By performing Ge deposition, at a constant rate $f/D = 4 \times 10^{-4}$, an island is observed to grow into the pit, as indicated by the three representative stages reported in the figure, corresponding to different amounts of material deposition $h_d = f \times t$.

During the initial stages, the main driving force to be considered is capillarity, favoring the transfer of the deposited material inside the pit, in order to minimize the exposed surface. However, this is partly contrasted by the wetting-energy contribution, which favors the increase of the film thickness, in order to reduce γ, according to Eq. (8). Elasticity is still not playing a significant role, as indicated by the rather uniform elastic energy density ρ, shown by the color map. More precisely, only a small relaxation, due to the pit geometry, can be recognized at the bottom.

As far as the process continues, strained material is accumulated into the pit. When the stored elastic energy is large enough, the growth of an island becomes favorable (see $h_d = 1.3$ nm). Indeed, despite the cost related to increasing the surface extension, the island geometry permits an enhanced strain relaxation, with respect to the flat configuration. Notice that, since material flows toward the pit from the surrounding regions, the onset for island growth is anticipated to a lower h_d if compared to the case of a flat substrate, so that the WL on the outer regions does not grow above the critical thickness h_c.

At first, the size of the island base is almost comparable to the wavelength λ_{ATG}, characteristic of the ATG instability for a flat film. However, as additional material is deposited (see $h_d = 1.7$ nm), the island grows larger by increasing both its amplitude, to better release strain (as in standard ATG model), and its base, climbing along the pit sidewalls. This permits to obtain the best compromise between the elastic relaxation and the minimization of the surface area. The progressive strain release is well evident in the elastic energy map. Moreover, the strain map for the ε_{xx} component is reported in Fig. 4(b). Evidently, most of the island volume is more relaxed than the WL, especially at the island top. Only at the borders of the island, highly compressive lobes appear. By comparing the strain map with the case of an analogous island on a flat substrate, also shown in Fig. 4(b), it looks quite evident that the pit provides an enhancement in the strain relaxation. In particular, the island top clearly exhibits an almost fully relaxed, or even tensile strained, region which extends on a larger volume towards the bottom of the pit. As explained in Ref. [32], this stabilization is provided by the presence of the inverted-pyramidal region below the island base, which transfers part of the strain to the substrate sidewalls, profiting of its compliance [58]. This effect is naturally accounted for in our strain calculations, as indicated by the presence of tensile lobes into the substrate below the pit.

A deeper insight on the mechanisms involved can be inferred by monitoring the energetics of the system during the evolution, as reported (by solid lines) in Fig. 5 for both the energy contributions and for the total free energy of the system. In particular, Fig. 5(a) shows the surface energy G_γ, integrated along the whole profile as given by the first term in Eq. (3). The elastic contribution, quantified by the elastic energy density averaged over the stressed film volume $\langle\rho\rangle$, is shown in Fig. 5(b). The behavior of the total system free energy G is reported in Fig. 5(c). It must be pointed out that the material redistribution, described by Eq. (1), is driven by the tendency to minimize the free energy at fixed volume. Nevertheless, deposition continuously increases the volume of strained material, so that the total energy is growing anyway. In order to better identify the conditions leading to the island growth into the pit, the trends observed in the simulation are compared with the reference case of conformal growth on the pit (dashed lines), where material redistribution is not allowed (e.g., because of low growth temperature [59] or high deposition rate). The energetic advantage offered by the island is made evident in Fig. 5(d), where the difference in free energy between the two cases, $\Delta G = G_{island} - G_{conformal}$, is reported.

Three different stages can be recognized. As shown in Fig. 5(a), the first part of the evolution (I) is characterized by a significant decrease in the surface energy that can be ascribed to the thickening of the WL, yielding an exponential decay in γ according to Eq. (8). An almost conformal growth characterizes this stage, except for an initial rounding of the sharp tip at the bottom of the pit, so that the energy is just slightly lower than the reference case.

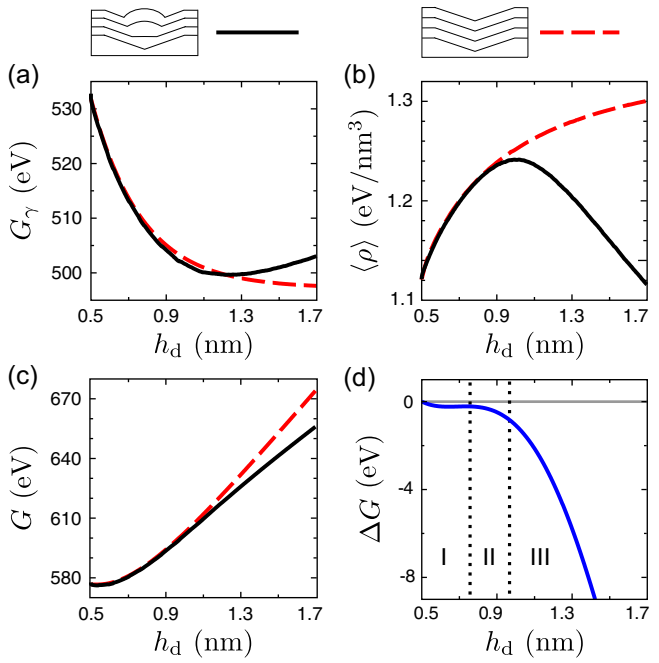

FIG. 5. Plot of the energy contributions for the evolution in Fig. 4 (solid line), compared to a conformal growth (dashed line). (a) Surface energy G_γ, corresponding to the first integral in Eq. (3) computed on the whole surface. (b) Elastic energy density ρ, averaged over the film volume. (c) Total free energy G including both film and substrate. (d) Difference in G between the two growth regimes here compared. I: quasiconformal growth; II: pit filling; III: islanding.

The advantage of making the WL thick contrasts the driving force toward pit filling. However, this effect decays exponentially as more material is accumulated on the WL, so that, later on, material flow into the pit becomes favored. At this stage (II), surface transport permits a reduction in the surface energy with respect to the conformal growth. Material accumulates into the pit, producing a flattening of its bottom [see $h_d = 0.9$ nm in Fig. 4(a)]. Stages I and II are essentially controlled by surface energy, but the elastic field is affected by the pit morphology. At variance from a tetragonally distorted flat film, characterized by a constant value ρ_t for the elastic energy density (equal to 1.38 eV/nm^3 for the case of Ge/Si here considered) independent of the film thickness, the presence of the corner regions at the rims and at the bottom of a pit induces a nonuniform strain field in the film, providing a better strain release. As observed in Fig. 4(b), this is not only due to the presence of the additional surfaces therein, but also to the strain repartitioning between the film and the substrate. These mechanisms of strain relaxation are effective only for a thin film, so that $\langle\rho\rangle$ converges to the tetragonal value ρ_t in the limit of thick conformal films, as illustrated in Fig. 5(b). However, the pit filling characterizing the evolution during stage II offers an alternative path for the strain relaxation so that, at some point, $\langle\rho\rangle$ is observed to decrease again.

The effect of strain relaxation becomes dominant during stage III, when the island grows into the pit, largely compensating the cost due to increasing the surface area. As made evident in Fig. 5(d), a significant lowering in G is then obtained with respect to the conformal film, thus proving that the growth of an island into the pit is a better pathway for the free-energy minimization.

B. Role of the growth conditions

In Sec. III A, the growth process has been analyzed for the optimal case of a single island growing into the pit. However, this is possible only for a well-defined range of growth conditions [28]. Indeed, it is true that the pit represents a preferential site for island growth, but in general this is not sufficient to prevent other islands to form outside.

According to our growth model [see Eq. (1)], a key parameter is the ratio f/D between the deposition flux and the surface mobility, i.e., the growth temperature, setting the diffusion length of the deposited material before being buried by the deposition of another layer. The effect of varying this parameter in the simulations is illustrated in Fig. 6. Profiles are reported for deposition of 2.3 nm with different f/D, on the same pattern used in Fig. 4.

For the lowest f/D ratio, material redistribution is unrestricted and the whole deposited volume above the WL can flow into the pit, contributing to the growth of a single island. By taking the f/D ratio three times larger ($f/D = 6 \times 10^{-4}$), the localization is still achieved, but material tends to accumulate on the WL far from the pit, as evidenced by the small slope at the borders of the plot. This indicates a

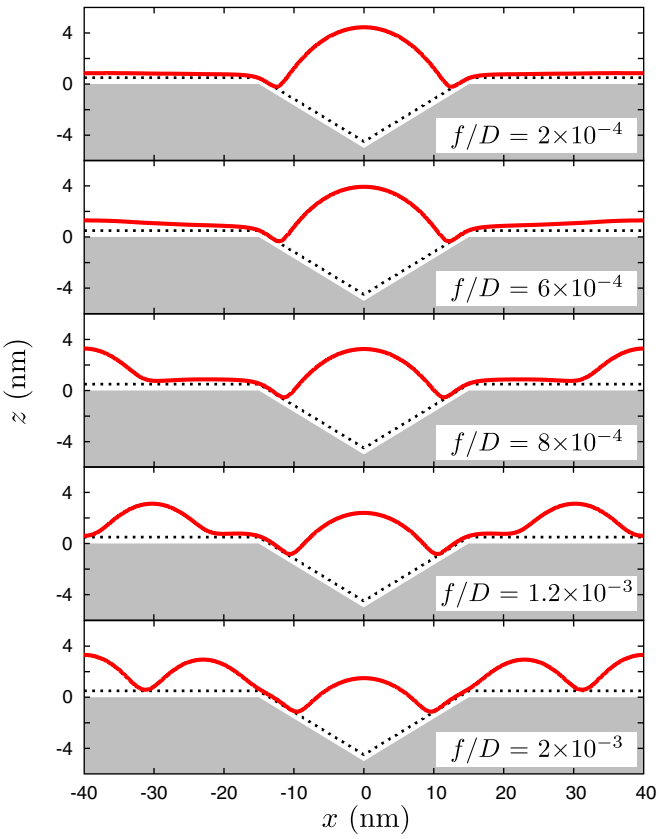

FIG. 6. Role of the deposition-to-diffusion ratio f/D in the growth. The initial condition (dotted lines) is a conformal film, 0.5 nm thick, with the same pit geometry of Fig. 4. Profiles are plotted after 2.3 nm deposition. Notice that, for the case $f/D = 6 \times 10^{-4}$, the WL is thicker at the borders of the cell.

shorter diffusion length, even if the pit is still able to capture most of the material. The limitation in the diffusion length becomes more dramatic when increasing further the f/D ratio, allowing for the growth of islands outside the pit. In particular, at $f/D = 8 \times 10^{-4}$, a single island appears at the border of the cell, i.e., at a distance where material is no more attracted toward the pit. A second island is formed on the flat region for the case at $f/D = 1.2 \times 10^{-3}$ because of the further reduction of the capture zone. Finally, at the largest f/D ratio here considered, a third island appears, so that the whole WL is covered.

The condition of high f/D represents a growth which is slightly affected by the presence of the pit. Indeed, the growth of the WL above the critical thickness allows for the formation of islands everywhere. Such a regime is close to the one predicted by the ATG theory for a flat substrate, where a small perturbation of the profile is supposed to develop randomly. However, in the simulations, the presence of the pit still plays a role by aligning the perturbation to the pit center, where a lower chemical potential is still present, yet not sufficient to drain material by capillarity. Notice that the base of the islands on the flat regions reflects the typical instability wavelength λ_{ATG}, while the island into the pit grows larger following the sidewalls.

It is now important to discuss the effect of the size of the pit in determining the optimal f/D ratio for a localized growth. In particular, in Fig. 6, the pit width has been chosen to accommodate only one island. However, this is not required to achieve ordering as shown in Fig. 7 for a pit twice larger, i.e., $\approx 4\lambda_{\mathrm{ATG}}$. Island positioning can still be controlled by tuning the f/D ratio. For a very low $f/D = 2 \times 10^{-4}$ ratio, a single island forms inside the pit, while the WL remains perfectly flat, thus indicating that all the deposited material is collected into the pit. However, when the ratio is increased to $f/D = 6 \times 10^{-4}$, which in Fig. 6 was sufficient to obtain a localized growth, a perturbation of the film profile is also activated on the flat regions. Moreover, for the largest f/D ratio, multiple islands are observed on the sidewalls of the pit [60]. This happens because the upper part of the sidewalls is far enough from the pit bottom to accumulate material and to grow above the critical WL thickness. Nevertheless, these islands are the smallest because their growth is slowed down by the strong competition with the larger island in the center of the pit. Interestingly, it must be pointed out that island growth into the pit becomes apparent almost at the same volume, i.e., at the same base width, obtained for the smaller pit as in Fig. 4. Consequently, if the pit width is chosen too small, the island is expected to form on top of it, only after complete filling.

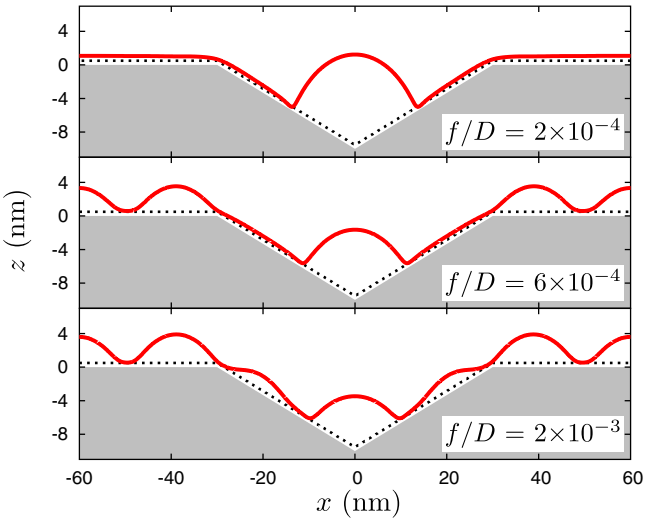

FIG. 7. Role of the flux for larger pits obtained by doubling the base and the depth of those in Fig. 6. The initial condition (dotted lines) is a conformal film 0.5 nm thick. Profiles are plotted after 2.3 nm deposition.

The analysis of the trends in Figs. 6 and 7 allows one to identify the extension of the capture zone of the island into the pit, which shrinks for higher f/D ratio. Evidently, if the pattern periodicity exceeds this length by at least $\sim\lambda_{\mathrm{ATG}}$, material is expected to accumulate above the WL, up to overtaking the critical thickness and forming islands out of the pit. On the other hand, literature studies [27] showed that if the capture zones of the pits overlap, at long times islands are expected to exchange material with each other and eventually undergo Ostwald ripening, leading to a loss in homogeneity. This behavior, not reproduced by the present simulations where a single pit is considered, introduces a restriction on the minimum distance between the pits or, correspondingly, on the f/D ratio, so that only intermediate f/D are expected to yield perfect ordering.

Profiles resulting from growth simulations depend on the deposition flux and hence they represent, in general, metastable states, eventually different from the equilibrium configuration. The possibility to follow a real kinetic path in the simulations is a great advancement with respect to simply considering equilibrium calculations, allowing to best compare with experiments, which are indeed out of equilibrium. However, it is crucial to assess what is the equilibrium condition toward which the system tends. This is investigated in Fig. 8, where annealing simulations (i.e., $f/D = 0$) are performed. Notice that the equilibrium condition here achieved does not necessarily correspond to the absolute minimum in energy but to the lowest one accessible by surface diffusion. In Fig. 8(a), the very same profile obtained for $f/D = 1.2 \times 10^{-3}$ in Fig. 6, characterized by islands both into the pit and on the flat region, is set as initial state. As shown, the material above the WL is transferred into the pit, reducing the volume of the islands outside, up to their disappearance. This is driven by the chemical potential at the surface, minimum at the top of the island in the pit. Therefore, islands outside the pit correspond to metastable states, formed during the growth, but not present in the minimum-energy configuration. It must be pointed out that the formation of islands out of the pit is possible also by performing annealing simulations as in the cases shown in Figs. 8(b) and 8(c) for both 30-nm and 60-nm wide pits, respectively. An initial conformal film, exceeding the critical WL thickness, is considered, matching the deposited material $h_{\mathrm{d}} = 2.3$ nm of Fig. 8(a). In both cases, the film instability first develops over the whole profile ($t = 500\ \tau$), inducing the formation of islands on the flat regions in-between the pits and even on the pit sidewalls for the largest geometry in Fig. 8(c). This behavior, similar to the cases of deposition at high f/D in Figs. 6 and 7, is however

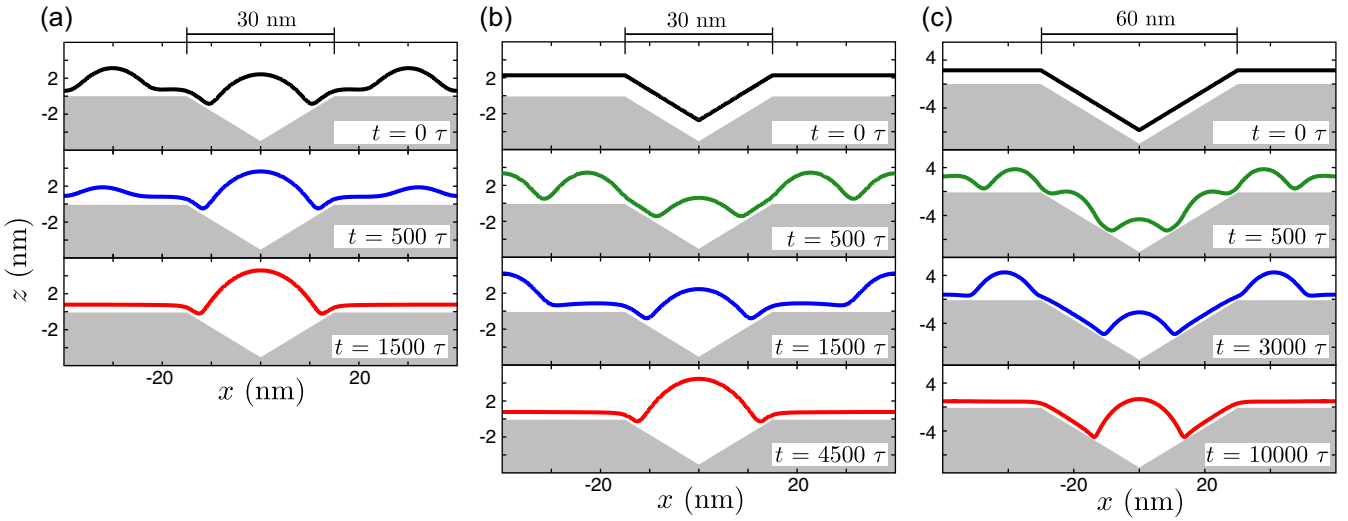

FIG. 8. Annealing simulations from different initial geometries. (a) Evolution of the profile obtained for $f/D = 1.2 \times 10^{-3}$ in Fig. 6. (b), (c) Evolution of a 2.3-nm-thick conformal film [corresponding to the deposited material in (a)] for (b) a 30-nm-wide pit as in Fig. 6, and (c) a 60-nm-wide pit as in Fig. 7. Notice that the resulting islands in (a) and (b) are identical, while the one in (c) is larger due to the additional volume available in the cell.

transitory. Indeed, by extending the annealing time, coarsening occurs in favor of the island at the pit bottom, profiting of its better strain relaxation. At the end of the process, only this single island survives, yielding the actual equilibrium profile, identical for the (a) and (b) cases of Fig. 8, despite the different initial conditions.

C. Pattern geometry and material properties

As discussed in Sec. III A, island growth into pits is favored both by capillarity and strain relaxation, profiting of the transfer of part of the elastic deformation to the substrate. These beneficial effects strongly depend on both the pattern geometry and the elastic properties of the substrate versus film materials.

Nowadays, experimental techniques [21,24,28] allow one to finely control the pit shape, so that different geometries should be considered. Growth simulations performed on V-shaped pits with different sidewall inclinations, at a small f/D ratio mimicking quasiequilibrium conditions, still follow the same evolution pathway discussed so far: first a partial pit filling followed by island growth therein.

The evolution of islands growing into pits with three different slopes is analyzed in Fig. 9. The pit has been set as wide as the simulation cell so to exclude any interaction with flat WL regions and to provide a direct correspondence of the island volume for all cases. As addressed in Sec. III A, at the onset of island growth, the typical base size $\sim\lambda_{ATG}$ is observed, without significant effects from the pit morphology. However, the volume required to fill the pit up to this level largely increases for steeper sidewalls, thus delaying the formation of the island to later stages. As made evident in Fig. 9(a), at a fixed deposition time (i.e., same deposited volume), an island formed within a shallow pit is in a more advanced development stage than one formed on a steeper geometry.

To better highlight the effect of the pit inclination on the island evolution, Fig. 9(b) reports the variation in time of its AR. The case of island growth on a flat substrate is also reported as reference (shifted along the h_d axis at the onset of island growth on the shallowest pit for a closer comparison). Due to the very low deposition flux here considered, the curves can be meant as tracing the equilibrium AR of the island grown in the pit as a function of its volume. As evident, the different sidewall inclination does not affect only the onset of island formation, but also its tendency to grow higher in AR, as indicated by the curve slopes. The steeper is the pit, the slower is the raise of the island AR.

This is made more clear when comparing the shape of islands of equal AR (different volume), grown in the three

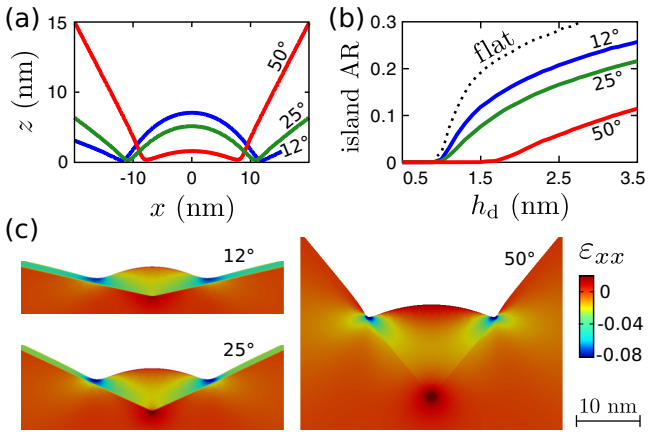

FIG. 9. Simulations of island growth into pits of different sidewalls inclination: 12°, 25°, and 50°. A low $f/D = 1 \times 10^{-4}$ is set. (a) Comparison of the profiles obtained at the same deposition time (vertical alignment is arbitrarily set). (b) Temporal evolution of the island AR. The curve for the case of an isolated island on a flat WL is shown by a dotted line (shifted at the onset of island growth for the shallowest pit). (c) Strain maps for the ε_{xx} component of islands at the same AR of 0.1. Only the central portion of the simulation cell (60 nm wide) is shown (in 1:1 ratio).

pits, as in Fig. 9(c). For the steepest pit the island appears quite rounded, while for the shallowest one the island is cusplike, similarly to the expectation on a flat substrate [61,62]. This reflects the stronger tendency toward a flat pit filling for steeper geometries. Indeed, the connection between the island and the WL along the sidewalls involves high curvature regions, thus favoring a more rounded shape. Moreover, in Ref. [32] it was shown that the inverted-pyramid region underneath provides additional strain relaxation proportionally to the sidewalls inclination, producing a significant lowering of the strain at the top of the island. This effect is naturally accounted for in our simulations, as indicated by the strain maps in Fig. 9(c). As a consequence, the gradients of chemical potential are reduced in the case of steeper pits and do not require the formation of high AR features to release strain, as observed in Fig. 9(b).

However, when comparing this trend with experimental data for different pit shapes, it is well evident that the validity of the model is limited to relatively shallow morphologies, with facet angles $\lesssim 30^\circ$. A larger variety of experimental behaviors emerges when considering steeper geometries. In particular, it has been shown that island formation on the rims of a pit might become favored with respect to the growth inside of it [25,28,32]. Experiments [24] also showed that for certain growth conditions, small pits (designed by focused ion beam) might play an opposite role in ordering the islands in-between each other. Even if theoretical studies [30,31], based on approaches similar to the one reported here, have been recently exploited to investigate this behavior, the reproduction of these trends is still beyond the capabilities of the present model. A large number of physical features have not been considered yet, such as surface anisotropy, in particular the strain stabilization of {105} facets [47], favoring spontaneous growth of pyramids even on flat, the role of anisotropic elastic constants in the definition of the WL energy, largely dependent on the facets and hence on pit sidewalls inclination, intermixing dynamics, kinetic effects, or even barriers [23], slowing down the transfer of material from the rims to the bottom of the pit, nucleation conditions [63]. Deposition is also expected to become quite nonuniform when considering high AR morphologies, eventually triggering the island growth on elevated regions [64]. A very recent work [65] even suggests that nonlinear elastic effects may explain the formation of islands around pits. All these contributions might play a role in changing the evolution with respect to the simple picture here discussed.

From this discussion it is evident how peculiar details of the system might produce a wide variety of behaviors, even for a simple, well-defined geometry as that of a pyramidal pit. Additional complexity can arise when changing the pattern geometry. For example, in Ref. [66] it was shown that island growth can be directed even on convex regions at the top of large stripes and mesas, due to the existence of local minima in the chemical potential at such locations. Nonetheless, the foot of these structures still represents the most favorable location enforced by capillarity, where islands are expected to develop and eventually dominate when close-to-equilibrium conditions are set, similarly to the case of the pits here analyzed.

Material properties are also expected to have an impact on the dynamics of pit filling and island growth. Results shown so far have been reported for the prototypical Ge/Si(001) case but can in principle be extended to other systems. First of all, while still considering SiGe, it is possible to tune the lattice misfit just by alloying, as Si and Ge are perfectly miscible for any composition. As a matter of fact, even when pure Ge is deposited on Si, at high temperature alloying is often unavoidable, injecting a significant fraction of Si within the growing islands [42]. While the actual dynamics of intermixing during the growth is not part of the present treatment [16–18], it is possible to inspect the evolution for an alloyed film (substrate) just by setting the proper misfit ε_m^{fs} and surface energy γ_f (γ_s). For ideal alloys (as SiGe), these can be easily approximated by exploiting Vegard's law. According to the ATG model, the major effect of changing the composition is a variation in the size of the island base, i.e., $\lambda_{ATG} \sim \gamma/\varepsilon_m^2$. A larger volume of strained material is then accumulated into the pit by capillarity, before observing the island growth. Still, the pit provides a better strain relaxation with respect to a flat substrate thus behaving as a preferential nucleation site. This holds true even if the pit is smaller than the expected λ_{ATG}, as illustrated in Fig. 10(a), where deposition of a 50-50 SiGe alloy ($\lambda_{ATG} \approx 60$ nm) is simulated on a 30-nm-wide pit. Evidently, the first two stages (here selected to match the same amounts of deposition leading to island growth in the case of pure Ge of Fig. 4) are just dominated by the tendency toward complete filling of the pit. Once this process is accomplished, material continues to preferentially accumulate on top of the pit region due to the better strain relaxation provided by the inverted pyramid below so that a modulation in the profile rises and finally leads to a proper island.

Recent studies have shown that porous silicon or silicon membranes might behave as compliant substrates [45,67], providing a better strain relaxation of the film. An even wider variety of elastic properties is possible by considering other heteroepitaxial systems. The effect of different elastic constants on the ATG instability for a planar configuration has been discussed in the literature [55]: stiffer substrates are responsible for a stabilization of the flat film configuration, increasing the critical thickness h_c and the instability wavelength λ_{ATG}.

This behavior becomes more complex when considering a pit-patterned substrate. In Fig. 10(b), a comparison of the growth of an island into a pit (AR = 1:6) is reported for two different substrates, made softer (left) and stiffer (right) than Si by scaling its elastic constants. As evident, at the early stages, pit filling is enhanced in the case of soft substrate so that an island is formed at the pit bottom and tends to grow following the pit sidewalls as already discussed. On the other hand, for the stiff case, the WL grows thicker and only at later stages the accumulation of material at the pit bottom induces the growth of an island. While the thicker WL is well consistent with the prediction on a flat substrate [55], the following evolution of the island is not. Indeed, the island on the soft substrate tends to climb along the pit sidewalls, increasing its base size, while in the case of stiff substrate the island base remains narrower and the growth favors higher AR. This is well evident in the last stage reported ($h_d = 3.0$ nm) where the island grown on the stiff substrate exceeds the height of the one on the soft substrate. The explanation for such a different behavior can be found in the different partitioning of the strain between the film and the substrate, made clear by the color maps in the figure. On the compliant substrate, a large part of the misfit strain is

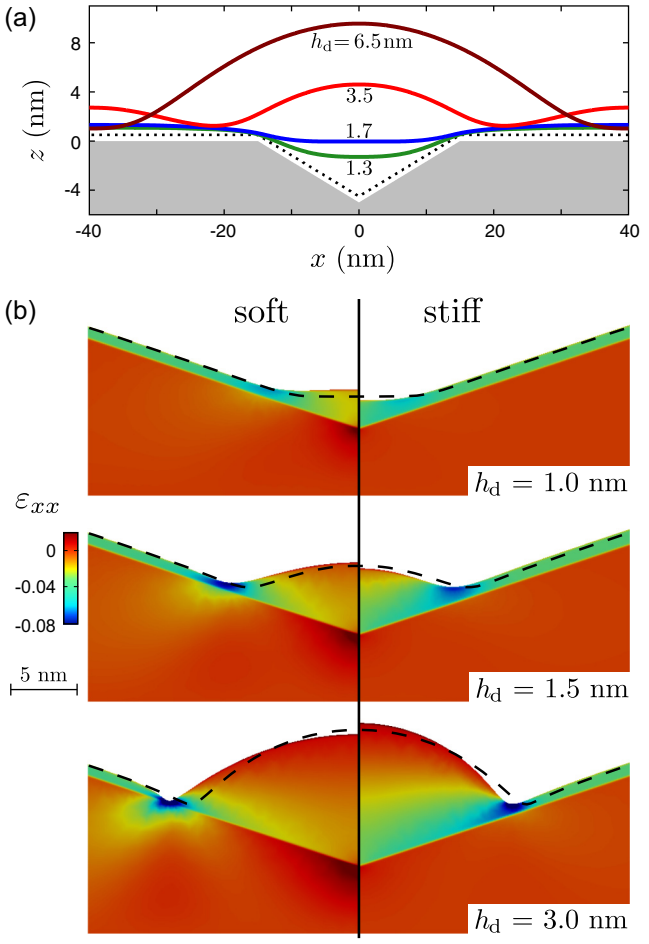

FIG. 10. Effects of different elastic properties. (a) Evolution sequence for a simulation performed with the same pattern and growth conditions of Fig. 4 but for the deposition of a 50-50 SiGe alloy. (b) Comparison of island growth into the pit for (left) a soft substrate, with $\mu_s = 20$ GPa, $\lambda_s = 23$ GPa, and (right) a stiff one, with $\mu_s = 236$ GPa, $\lambda_s = 277$ GPa (values are obtained by an arbitrary scaling of the Si Young modulus). Misfit and surface properties are the same of Ge/Si. The dashed lines represent the corresponding surface profiles for the case with Si substrate. The strain component ε_{xx} is shown by the color map. Simulations are performed on a 60-nm-wide pit, as large as the simulation cell. Only the central region is reported (in 1:1 ratio). $f/D = 1 \times 10^{-4}$.

transferred to the substrate through the pit sidewalls, allowing the island to significantly relax strain even for a lower AR. This mechanism is no more possible on the stiff substrate, which remains practically undeformed as indicated by the uniform color map. In this case, the island does not profit much of the pit morphology, so that strain can be released just by growing steeper, as on a flat substrate.

D. 3D results

The results discussed in the previous sections are expected to be valid for the general description of the mechanisms behind the growth process. However, a more realistic description of the experimental system requires to properly account for its 3D geometry. This affects both the system energetics and the dynamics of material transfer. Pits are typically not symmetric by rotation (e.g., inverted pyramids), so that their shape cannot be modeled just by a 2D section. Moreover, their arrangement on the substrate is inherently 3D. For example, in a squared lattice of pits, as typical in experiments, differences in the amount of material flowing toward the pit are expected between the directions of nearest neighbors and those for second-nearest neighbors, the latter corresponding to a much larger flat region.

The PF model discussed here, as well as its implementation, can be straightforwardly applied to the simulation of actual 3D domains, just by extending the φ and c fields to the third dimension. Obviously, the computational cost is greatly increased so that a lower spatial resolution has to be considered in the simulations. In particular, larger interface widths ϵ have been set for both the free-surface (0.7 nm) and the film-substrate interface (0.4 nm). Pits have been modeled as inverted pyramids, with the same 1:6 AR considered in the 2D simulations, matching the typical shape observed in the experiments. To reduce the computational cost, only a quarter of a pit has been simulated, in the assumption of symmetry with respect to its center.

In Figs. 11(a) and 11(b), 3D simulation results are reported for representative stages of island growth. Evidently, the overall behavior is fully consistent with all the previous modeling in 2D (see, e.g., Fig. 4): material is preferentially accumulated into the pit and hence an island starts to grow therein. The major difference between 2D and 3D simulations is due to the quantitative values of both surface energy (i.e.. profile curvatures) and strain relaxation, which here are more representative of the actual system, properly considering the finiteness of the pits and islands in all directions. As for the 2D cases, the localization of the island is related to the extent of material transfer from the flat regions into the pit. In particular, a low enough f/D ratio is required to maintain the WL thickness below the critical value h_c during the whole process, as in the case of Fig. 4. At variance from the 2D case, the pit capture zone is expected to depend quadratically on the distance from its center, so that the volume flowing into the pit is larger than the one expected for a 2D infinite groove, promoting the island growth.

The pit arrangement on the substrate, as well as the specific pit 3D morphology, might also influence the actual evolution. This is made evident in Fig. 11(c), reporting the contour lines for selected profile heights at different evolution stages. Indeed, the pit filling and the subsequent island growth reflect the squared symmetry of the initial pit structure. More precisely, the edges of the inverted pyramid behave as additional grooves, inducing the accumulation of material by capillarity, yielding an apparent rotation in the shape of the pit. This phenomenon is more evident at the early stages and for larger pits, with longer sidewalls. However, as soon as the island grows in AR, it loses any correlation with the pit shape and tends to the characteristic cusplike morphology, expected for isotropic surface and elastic energy.

IV. CONCLUSIONS

In this work, a phase-field approach is exploited for the simulation of heteroepitaxial growth on pit-patterned substrates. The method is devised in a general way, allowing for

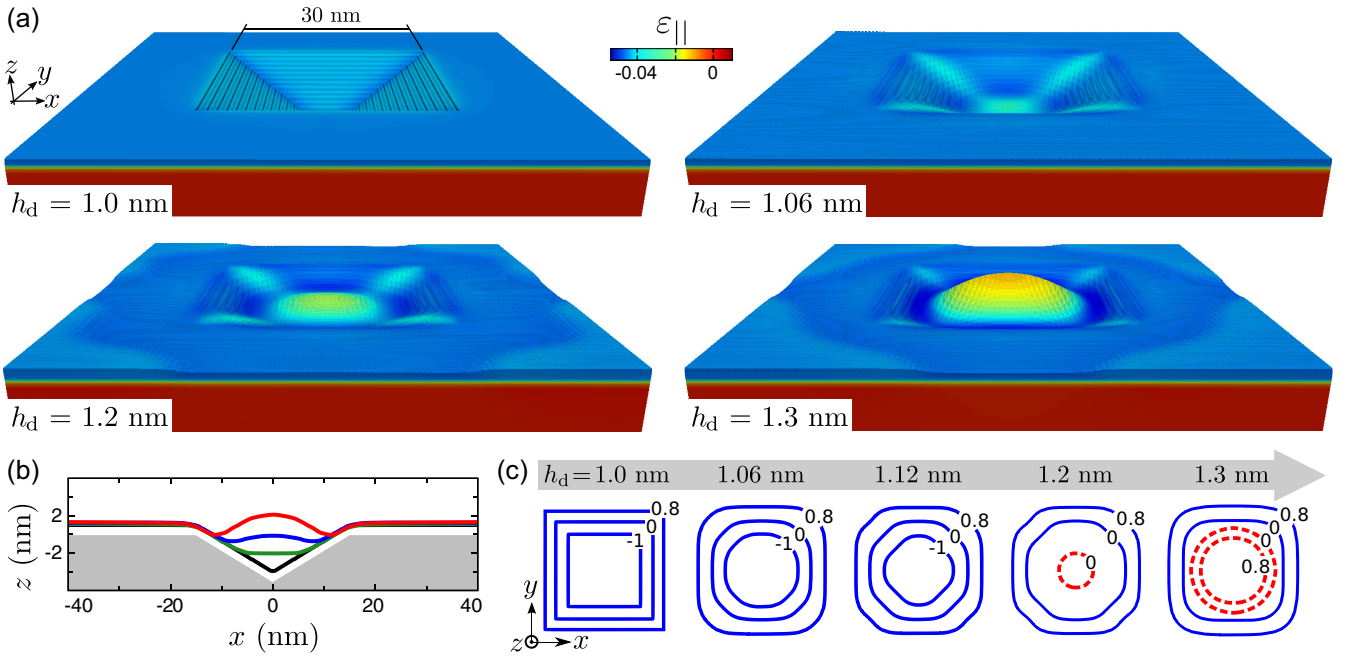

FIG. 11. 3D simulation of island growth on a pit-patterned substrate. A 30-nm-wide pit, with the shape of an inverted pyramid of AR 1:6 and periodicity of 80 nm, is considered. (a) Perspective views of representative evolution stages, reporting the in-plane strain field $\varepsilon_{||} = (\varepsilon_{xx} + \varepsilon_{yy})/2$ by color map (a portion of the simulation cell is shown, stretched by a factor 1.5 along z). Profiles are clipped at $\varphi = 0.9$. (b) Cross-section profiles along the x direction through the pit center for the four stages shown in (a). (c) Elevation contour lines, in top view, for different stages of the evolution. Reported values correspond to the profile height z with respect to the substrate level on the flat regions. Solid and dashed strokes are used for lines where z is decreasing or increasing, respectively, moving toward the center.

a proper description of the substrate geometry and properties and relies on the accurate calculation of the strain field by finite-element method.

Simulations have been performed for different growth parameters. In particular, it has been shown that close-to-equilibrium conditions favor the island localization within the pits, reflecting their enhanced stability due to both capillarity and elasticity. Simulations are observed to qualitatively capture the main trends observed in the experiments. Additional work will be devoted to extend the model in order to tackle further realistic effects such as elastic and surface anisotropy [14,68] or intermixing [69,70].

Finally, it must be noted that the model here introduced is not restricted to pit morphologies. Indeed, the high flexibility offered by the implicit description of both the film and substrate geometries permits to straightforwardly tackle whatever arbitrary pattern geometry. Our approach could then be exploited for investigating heteroepitaxial growth on other systems of interest, e.g., curved profiles as stripes or mesas [66], pillared structures [64], membranes [45].

ACKNOWLEDGMENTS

We kindly acknowledge technical support from M. Salvalaglio (University of Milano-Bicocca), R. Backofen, and A. Voigt (TU Dresden).

[1] Y.-W. Mo, D. E. Savage, B. S. Swartzentruber, and M. G. Lagally, Phys. Rev. Lett. **65**, 1020 (1990).
[2] D. J. Eaglesham and M. Cerullo, Phys. Rev. Lett. **64**, 1943 (1990).
[3] D. Leonard, K. Pond, and P. M. Petroff, Phys. Rev. B **50**, 11687 (1994).
[4] J. Stangl, V. Holý, and G. Bauer, Rev. Mod. Phys. **76**, 725 (2004).
[5] R. J. Asaro and W. A. Tiller, Metall. Trans. A **3**, 1789 (1972).
[6] M. A. Grinfeld, J. Nonlinear Sci. **3**, 35 (1993).
[7] D. Srolovitz, Acta Metall. **37**, 621 (1989).
[8] J. Tersoff, B. J. Spencer, A. Rastelli, and H. von Känel, Phys. Rev. Lett. **89**, 196104 (2002).
[9] R. Bergamaschini, M. Salvalaglio, R. Backofen, A. Voigt, and F. Montalenti, Adv. Phys. X (2016), doi:10.1080/23746149.2016.1181986.
[10] C. H. Chiu and H. J. Gao, Mater. Res. Soc. Symp. Proc. **356**, 33 (1995).
[11] B. J. Spencer, Phys. Rev. B **59**, 2011 (1999).
[12] M. S. Levine, A. A. Golovin, S. H. Davis, and P. W. Voorhees, Phys. Rev. B **75**, 205312 (2007).
[13] J.-N. Aqua, T. Frisch, and A. Verga, Phys. Rev. B **76**, 165319 (2007).
[14] T. Takaki, T. Hasebe, and Y. Tomita, J. Cryst. Growth **287**, 495 (2006).

[15] B. J. Spencer, P. W. Voorhees, and J. Tersoff, Phys. Rev. Lett. **84**, 2449 (2000).
[16] Y. Tu and J. Tersoff, Phys. Rev. Lett. **93**, 216101 (2004).
[17] Y. Tu and J. Tersoff, Phys. Rev. Lett. **98**, 096103 (2007).
[18] R. Bergamaschini, J. Tersoff, Y. Tu, J. J. Zhang, G. Bauer, and F. Montalenti, Phys. Rev. Lett. **109**, 156101 (2012).
[19] F. Jonsdottir and L. Freund, Mech. Mater. **20**, 337 (1995).
[20] J. J. Zhang, A. Rastelli, H. Groiss, J. Tersoff, F. Schäffler, O. G. Schmidt, and G. Bauer, Appl. Phys. Lett. **95**, 183102 (2009).
[21] E. Lausecker, M. Brehm, M. Grydlik, F. Hackl, I. Bergmair, M. Mühlberger, T. Fromherz, F. Schäffler, and G. Bauer, Appl. Phys. Lett. **98**, 143101 (2011).
[22] G. Biasiol and E. Kapon, Phys. Rev. Lett. **81**, 2962 (1998).
[23] Z. Zhong, J. Stangl, F. Schäffler, and G. Bauer, Appl. Phys. Lett. **83**, 3695 (2003).
[24] A. Pascale, I. Berbezier, A. Ronda, and P. C. Kelires, Phys. Rev. B **77**, 075311 (2008).
[25] M. Grydlik, M. Brehm, F. Hackl, H. Groiss, T. Fromherz, F. Schäffler, and G. Bauer, New J. Phys. **12**, 063002 (2010).
[26] M. Grydlik, M. Brehm, F. Hackl, F. Schäffler, G. Bauer, and T. Fromherz, Phys. Rev. B **88**, 115311 (2013).
[27] R. Bergamaschini, F. Montalenti, and L. Miglio, Nanoscale Res. Lett. **5**, 1873 (2010).
[28] M. Grydlik, G. Langer, T. Fromherz, F. Schäffler, and M. Brehm, Nanotechnology **24**, 105601 (2013).
[29] P. Liu, Y. W. Zhang, and C. Lu, Appl. Phys. Lett. **90**, 071905 (2007).
[30] J.-N. Aqua and X. Xu, Phys. Rev. E **90**, 030402 (2014).
[31] J.-N. Aqua and X. Xu, Surf. Sci. **639**, 20 (2015).
[32] G. Vastola, M. Grydlik, M. Brehm, T. Fromherz, G. Bauer, F. Boioli, L. Miglio, and F. Montalenti, Phys. Rev. B **84**, 155415 (2011).
[33] P. Liu, C. Lu, and Y. W. Zhang, Phys. Rev. B **76**, 085336 (2007).
[34] H. Wang, Y. Zhang, and F. Liu, J. Appl. Phys. **104**, 054301 (2008).
[35] K. Kassner, C. Misbah, J. Müller, J. Kappey, and P. Kohlert, Phys. Rev. E **63**, 036117 (2001).
[36] A. Rätz, A. Ribalta, and A. Voigt, J. Comput. Phys. **214**, 187 (2006).
[37] L. G. Wang, P. Kratzer, M. Scheffler, and N. Moll, Phys. Rev. Lett. **82**, 4042 (1999).
[38] S. M. Wise, J. S. Lowengrub, J. S. Kim, K. Thornton, P. W. Voorhees, and W. C. Johnson, Appl. Phys. Lett. **87**, 133102 (2005).
[39] J. J. Eggleston and P. W. Voorhees, Appl. Phys. Lett. **80**, 306 (2002).
[40] D. J. Seol, S. Y. Hu, Z. K. Liu, L. Q. Chen, S. G. Kim, and K. H. Oh, J. Appl. Phys. **98**, 044910 (2005).
[41] L. Huang, F. Liu, G.-H. Lu, and X. G. Gong, Phys. Rev. Lett. **96**, 016103 (2006).
[42] G. Capellini, M. De Seta, and F. Evangelisti, Appl. Phys. Lett. **78**, 303 (2001).
[43] L. Onsager, Phys. Rev. **37**, 405 (1931).
[44] L. Onsager, Phys. Rev. **38**, 2265 (1931).
[45] J.-N. Aqua, L. Favre, A. Ronda, A. Benkouider, and I. Berbezier, Cryst. Growth Des. **15**, 3399 (2015).
[46] C. Gugenberger, R. Spatschek, and K. Kassner, Phys. Rev. E **78**, 016703 (2008).
[47] G.-H. Lu, M. Cuma, and F. Liu, Phys. Rev. B **72**, 125415 (2005).
[48] G.-H. Lu and F. Liu, Phys. Rev. Lett. **94**, 176103 (2005).
[49] Y. Pang and R. Huang, Phys. Rev. B **74**, 075413 (2006).
[50] M. Brehm, F. Montalenti, M. Grydlik, G. Vastola, H. Lichtenberger, N. Hrauda, M. J. Beck, T. Fromherz, F. Schäffler, L. Miglio, and G. Bauer, Phys. Rev. B **80**, 205321 (2009).
[51] J.-N. Aqua, T. Frisch, and A. Verga, Phys. Rev. E **81**, 021605 (2010).
[52] R. Bergamaschini, M. Brehm, M. Grydlik, T. Fromherz, G. Bauer, and F. Montalenti, Nanotechnology **22**, 285704 (2011).
[53] S. Vey and A. Voigt, Comput. Vis. Sci. **10**, 57 (2007).
[54] T. Witkowski, S. Ling, S. Praetorius, and A. Voigt, Adv. Comput. Math. **41**, 1145 (2015).
[55] B. J. Spencer, P. W. Voorhees, and S. H. Davis, Phys. Rev. Lett. **67**, 3696 (1991).
[56] D. J. Godbey, J. V. Lill, J. Deppe, and K. D. Hobart, Appl. Phys. Lett. **65**, 711 (1994).
[57] B. Li, J. Lowengrub, A. Rätz, and A. Voigt, Commun. Comput. Phys. **6**, 433 (2009).
[58] R. Kukta and L. Freund, J. Mech. Phys. Solids **45**, 1835 (1997).
[59] M. Asai, H. Ueba, and C. Tatsuyama, J. Appl. Phys. **58**, 2577 (1985).
[60] R. V. Kukta and D. Kouris, J. Appl. Phys. **97**, 033527 (2005).
[61] C. Cheng-Hsin and G. Huajian, Int. J. Solids Struct. **30**, 2983 (1993).
[62] H. Gao and W. D. Nix, Annu. Rev. Mater. Sci. **29**, 173 (1999).
[63] H. Hu, H. Gao, and F. Liu, Phys. Rev. Lett. **109**, 106103 (2012).
[64] S. Wang, T. Zhou, D. Li, and Z. Zhong, Sci. Rep. **6**, 28872 (2016).
[65] H. Hu, X. Niu, and F. Liu, Nano Lett. **16**, 3919 (2016).
[66] B. Yang, F. Liu, and M. G. Lagally, Phys. Rev. Lett. **92**, 025502 (2004).
[67] F. Liu, M. Huang, P. P. Rugheimer, D. E. Savage, and M. G. Lagally, Phys. Rev. Lett. **89**, 136101 (2002).
[68] M. Salvalaglio, R. Backofen, R. Bergamaschini, F. Montalenti, and A. Voigt, Cryst. Growth Des. **15**, 2787 (2015).
[69] X. Liang, Y. Ni, and L. He, Comput. Mater. Sci. **48**, 871 (2010).
[70] R. Backofen, R. Bergamaschini, and A. Voigt, Philos. Mag. **94**, 2162 (2014).